Auxetic mechanical metamaterials to enhance sensitivity of stretchable strain sensors

Jiang, Ying; Liu, Zhiyuan; Matsuhisa, Naoji; Qi, Dianpeng; Leow, Wan Ru; Yang, Hui; Yu, Jiancan; Chen, Geng; Liu, Yaqing; Wan, Changjin; Liu, Zhuangjian; Chen, Xiaodong

2018

Auxetic Mechanical Metamaterials to Enhance Sensitivity of Stretchable Strain Sensors

Ying Jiang, Zhiyuan Liu, Naoji Matsuhisa, Dianpeng Qi, Wan Ru Leow, Hui Yang, Jiancan Yu, Geng Chen, Yaqing Liu, Changjin Wan, Zhuangjian Liu,* Xiaodong Chen*

Prof. X. Chen, Y. Jiang, Z. Liu, Dr. N. Matsuhisa, Dr. D. Qi, Dr. W. R. Leow, Dr. H. Yang, Dr. J. Yu, G. Chen, Dr. Y. Liu, Dr. C. Wan
Innovative Centre for Flexible Devices (iFLEX), School of Materials Science and Engineering, Nanyang Technological University, 50 Nanyang Avenue, 639798 Singapore
E-mail: chenxd@ntu.edu.sg
Webpage: http://www.ntu.edu.sg/home/chenxd/

Dr. Z. Liu
Institute of High Performance Computing, Agency for Science, Technology and Research, 1 Fusionopolis Way, 138632, Singapore
E-mail: liuzj@ihpc.a-star.edu.sg

Abstract

Stretchable strain sensors possess a pivotal role in wearable devices, soft robotics and Internet of Things, yet these viable applications, which require subtle strain detection under various strain, are often limited by low sensitivity.   This inadequate sensitivity stems from the Poisson's effect in conventional strain sensors, where stretched elastomer substrates expand in longitudinal direction, but compress transversely.   In stretchable strain sensors, expansion separates the active materials and contributes to sensitivity, while Poisson compression squeezes active materials together, and thus intrinsically limits the sensitivity.   Alternatively, auxetic mechanical metamaterials behave 2D expansion in both directions, due to their negative structural Poisson's

ratio.   Herein, we demonstrate that such auxetic metamaterials can be incorporated into stretchable strain sensors to significantly enhance the sensitivity.   Compared to conventional sensors, sensitivity is greatly elevated with a 24-fold improvement. This sensitivity enhancement is due to the synergistic effect of reduced structural Poisson's ratio and strain concentration.   Furthermore, microcracks are elongated as an underlying mechanism, verified by both experiments and numerical simulations. This strategy of employing auxetic metamaterials could be further applied to other stretchable strain sensors with different constituent materials.   Moreover, it paves the way for utilizing mechanical metamaterials into a broader library of stretchable electronics.

Stretchable strain sensors, which transduce mechanical excitation into readable electrical or optical signals, play an important role in the emerging area of wearable devices,[1-6] healthcare monitoring,[7-10] soft robotics[11-14] and electronic skins.[15-17] For instance, stretchable strain sensors on neck muscles benefits diagnostic of damaged vocal cords, respiratory disorder and throat cancer,[18] while those on human wrist assist tremor detection in epilepsy and Parkinson's disease.[19]   In order to be viably employed in these applications, stretchable strain sensors must exhibit excellent performance in three crucial parameters: sensitivity, stretchability and cyclic durability.   In particular, sensitivity is of extreme importance, as it allows for precise detection of minute movements such as in the case of phonation vibration, thus providing exhaustive information for accurate diagnosis or analysis even under

2

stretching. The sensitivity of resistive stretchable strain sensors is defined by the gauge factor GF = $(\triangle R/R_0)/\varepsilon$, in which $\triangle R/R_0$ refers to relative resistance change and ε refers to tensile strain. However, it still remains a big challenge to achieve high sensitivity (gauge factor$\geq$50)[20] under large strain (e.g. 5.5% for hand motion detection),[21] which is required for practical implementation.[22-26]

Typically, resistive stretchable strain sensors are composed of conductive active materials, and thin film elastomer substrate or matrix.[27-32] To solve the challenge of sensitivity, most of the research focuses on changing and optimizing active materials, yet the achievable sensitivity still remains limited.[33-37] The reason of inadequate sensitivity is that thin film elastomer in conventional strain sensors endures transverse Poisson compression under stretching. As incompressible material, conventional thin film elastomer exhibits Poisson's ratio of 0.5.[38] Under stretching, it expands in longitudinal direction, but compresses in transverse direction. Microscopically, sensitivity of strain sensors depends on the separation degree of conductive active materials.[39-41] Expansion moves the active materials away from each other and contributes to sensitivity, while compression squeezes active materials and produces an inverse response. Thus sensitivity induced by longitudinal stretching is counteracted by transverse Poisson compression, which intrinsically limits the sensitivity (**Scheme 1**a). Therefore, how to regulate and reduce the conventional transverse Poisson compression under stretching remains a critical issue for sensitivity enhancement.

Thus, we sought to significantly enhance sensitivity of stretchable strain sensors

3

through the incorporation of auxetic mechanical metamaterials, which endure expansion in both longitudinal and transverse directions under stretching (Scheme 1b). Mechanical metamaterials, by virtue of their artificial structures rather than composition, can be endowed with extraordinary mechanical behaviors including negative structural Poisson's ratio,[42-45] compressibility tuning ability,[46,47] mechanical instability,[48] as well as strong yet lightweight properties[49,50]. Among these, auxetics with negative structural Poisson's ratio is one of the most important subfield in mechanical metamaterials.[51] The structural Poisson's ratio of conventional thin film and auxetics is demonstrated by normalized transverse displacement $D_\perp$ calculated from finite element analysis (FEA), under 0 to 60% nominal strain (Scheme 1c). Here the negative and positive value of $D_\perp$ represents transverse compression and expansion respectively, and structural Poisson's ratio ν is defined as $\nu = -D_\perp/D_\parallel$ ($D_\parallel$ is longitudinal displacement). It can be observed that conventional thin film structure and auxetics exhibit a positive and negative structural Poisson's ratio, respectively. In contrary to conventional Poisson compression, bi-directional expansion in auxetics promotes the separation degree of active materials, thus is promising to enhance sensitivity of stretchable strain sensors.

To this end, we rationally designed a highly-sensitive stretchable strain sensor, as illustrated in Scheme 1d, which comprises a 1-unit auxetic metamaterial structure. The sensor is composed of conductive single-wall carbon nanotube (SWCNT) network on polydimethylsiloxane (PDMS) thin film, with a PDMS auxetic frame.

4

This auxetic frame regulates the structural Poisson's ratio and transverse displacement in conductive SWCNT area. The strain sensing process occurs via the following: under stretching, microcracks originate and propagate within conductive SWCNT network, which block the otherwise fluent electron pathway and change the electrical resistance.[52-56] We were able to greatly increase the gauge factor to ~835 under 15% nominal tensile strain, which is ~24 fold improvement over conventional sensors (~35). This sensitivity improvement stems from synergistic effect of reduced structural Poisson's ratio and strain concentration, both induced by auxetic mechanical metamaterials. As an underlying mechanism, microcracks are elongated by auxetic metamaterials, which was revealed by scanning electron microscope (SEM) images and numerical simulations. As proof of concept, we demonstrated the detection of human radial pulse wave with high signal-to-noise ratio (~105 dB). This strategy for sensitivity enhancement is independent of constituent materials, and can be further employed to other stretchable strain sensors. Furthermore, it provides a new perspective to utilize the unusual, extraordinary properties of mechanical metamaterials into stretchable electronics.

Having established the rational design of auxetic structures in stretchable strain sensors, we employ fabrication process of 3D printing-assisted molding in conjunction with SWCNT self-spinning method[57] (Figure S1, Supporting Information). By tuning side length of auxetic frame, which could be easily achieved via 3D printing, the structural Poisson's ratio of auxetic sensors is regulated from 0.41 to 0.19 (Figure S2a, b Supporting Information), which was proven by

displacement distribution from FEA simulation.   The thickness of whole device consists of auxetic frame thickness and thin film thickness (Figure S2c, d Supporting Information).   The reduced structural Poisson's ratio in auxetic sensors stems from the combination of auxetic frame and thin film substrate, which is also proven by actual photos before and after stretching (Figure S3 Supporting Information).   As non-auxetic control, a conventional flat strain sensor without auxetic frame was employed (referred to as flat sensor henceforth), whose structural Poisson's ratio is 0.5 as discussed before.   The sensitivity of auxetic sensors with different structural Poisson's ratio was demonstrated using tensile test of 15% nominal strain (**Figure 1**a, b).   With structural Poisson's ratio of 0.5, relative resistance change and average gauge factor of conventional flat sensors only reached ~6 and ~35 respectively.   This value of sensitivity is consistent with our previous study.[57]   In sharp contrast, strain sensors based on auxetic metamaterials displayed much larger relative resistance change.   With structural Poisson's ratio of 0.41, 0.25 and 0.19, average gauge factor in auxetic sensors was enhanced to ~393, ~433 and ~835, respectively.   Compared with conventional flat strain sensors, our auxetic metamaterial strain sensors demonstrate high sensitivity as high as a 24-fold enhancement, and such sensitivity enhancement is robustly responsive to structural Poisson's ratio.

Besides sensitivity, it's also important to achieve cyclic durability in stretchable strain sensors, which represents the ability to maintain electrical function and mechanical integrity under long-term cycling.   The stretchable strain sensors based on auxetic metamaterials exhibit good cyclic durability, under more than 2,000

6

consecutive loading and unloading cycles (Figure 1c). The relative resistance change of different cycles under 15% tensile strain shows high degree of similarity (Figure 1d). The maximum relative resistance change is 137.5 for 1st cycle, and remained 128.6 for 2,000th cycle. In addition, average gauge factor under different tensile strain range (0-2%, 2-5%, 5-15%) shows little difference, indicating its good linearity (Figure S4, Supporting Information). Furthermore, the strain sensing performance of stretchable strain sensors also relies heavily on stretchability, since it needs to accommodate the whole strain range in practical application. Maximum stretchability of our auxetic strain sensor achieves 98%, with relative resistance change of ~4600 at breaking point (Figure S5a, Supporting Information). Since human skin accommodates body movement with stretchability up to 30%,[58] this maximum stretchability fulfills the requirements for skin-mounted wearable devices. The stretchability is probably limited by small defects from fabrication process (Figure S5b, Supporting Information), thus can be further improved. Additionally, cyclic durability under 30% tensile strain was maintained, proven by more than 2,000 consecutive loading and unloading cycles (Figure S6, Supporting Information). Performance comparison with other representative stretchable strain sensors further shows the advantages of auxetic strain sensors (Figure S7, Supporting Information). It has been proved that auxetic strain sensors can achieve high gauge factor and stretchability at the same time, as well as good cyclic durability.

In addition, since the size requirement of stretchable strain sensors depends on specific application, it's necessary to maintain the sensor performance after scaling

the sensor size.   Programmability of 3D printing method allows this size scaling, thus auxetic sensors were fabricated with 0.512 and 0.125 of the original volume. Also, auxetic sensors composed of a 5-unit auxetic array were fabricated, where the volume of each unit is 0.03125 of the original value (Figure S8, Supporting Information).   All of the scaled and arrayed strain sensors achieved high gauge factor of >500, which validates the sensor flexibility to fulfill practical requirements of multifarious sizes.

Next, we investigate the sensitivity in various strain range of auxetic strain sensors, to suggest their competence in detecting small deformation even under stretching status.   Three control strain sensors were employed, including pillar and square sensors with replaced auxetic frame, and the conventional plank sensors (Figure S9, Supporting Information).   The area of whole sensor and conductive SWCNT network are kept the same as in auxetic sensors.   Relative resistance change of auxetic sensors within 25 tensile cycles is much larger than all non-auxetic control (**Figure 2**a).   Here local gauge factor (LGF) is defined as the slope of relative resistance change curve:

$$\mathrm{LGF}(\varepsilon) = \frac{f(\varepsilon) - f(\varepsilon_0)}{\Delta\varepsilon} \tag{1}$$

where $f(\varepsilon) = \Delta R(\varepsilon)/R_0$ represents the relative resistance change curve, and ε represents tensile strain.   The difference between GF and LGF lies in the strain range, with $0 \sim \varepsilon$ in the former, and $(\varepsilon - \Delta\varepsilon) \sim (\varepsilon + \Delta\varepsilon)$ in the latter.   LGF plays a vital role in practical applications since strain sensors often work under pre-stretching status.   Stretchable strain sensor based on auxetic metamaterials exhibits LGF of 21.3, 7.2 and 4.4 at 3%,

9%, 15% tensile strain (Figure 2b), which indicates high sensing ability for subtle movement $\triangle\varepsilon$ at large strain.   In sharp contrast, LGF in all non-auxetic strain sensors are 1-2 orders of magnitude lower than auxetic ones.   These observations demonstrate that in varied strain range, strain sensors based on auxetic metamaterials possess unparalleled sensitivity over non-auxetic ones.

Strain distribution from FEA simulation allows insights into the auxetic/non-auxetic frames, revealing the regulatory effects of strain re-distribution and concentration (Figure 2c).   Bottom view with the underlying frames is adopted here, with 15% nominal strain applied in vertical direction.   In our simulation, the highlighted area lies in middle conductive SWCNT network, since it serves as the resistance testing region.   It is evident that both auxetics and pillar strain sensors exhibits strain re-distribution and concentration in the highlighted SWCNT area, while square and plank strain sensors show a nearly uniform strain distribution. Strain concentration ε_c in SWCNT area is further calculated from FEA (Figure 2d). Obvious differences are observed in ε_c, with 32%, 32%, 20% and 18% in auxetic, pillar, square and plank strain sensors respectively.   However, auxetic strain sensors exhibit average gauge factor as high as ~835, although its ε_c is similar to non-auxetic pillar sensors.   Within three non-auxetic control sensors, average gauge factor only reaches ~108, ~35 and ~35 of pillar, square and plank sensors respectively.   It can be concluded that the sensitivity improvement by auxetic metamaterials can be attributed to two factors: reduced structural Poisson's ratio as a main reason, and strain concentration as a secondary reason.

9

To investigate the underpinning working mechanism of auxetic metamaterial strain sensors, SEM images of SWCNT area were taken under 15% vertical strain (**Figure 3**a-b). Microcrack pattern was observed in large area (Figure S10, Supporting Information), and enlarged images clearly demonstrate the fracture of SWCNT network due to microcrack opening (Figure 3a, b inset). Auxetic metamaterial sensor displays longer microcracks, which nearly cut through the whole image (27.7 μm in average). On the contrary, flat sensor exhibits shorter microcracks with average of 14.8 μm (Figure S11, Supporting Information). Two numerical simulations were employed to build a holistic model, explaining the sensitivity enhancement based on microcrack theory. The first simulation of voltage drop elucidates why long microcrack length leads to high gauge factor of stretchable strain sensors (Figure 3e, f). This phenomenological model is based on a previous work of Wagner's group,[59] using experimental SEM images. Here the SEM images were turned binary from gray scale, and voltage distribution was calculated after applying voltage drop on both top and down sides (Figure S12, Supporting Information). It is clearly shown that the voltage distribution of auxetic strain sensors drop much faster than flat sensors, representing a larger resistance under stretching. This lager resistance is consistent with intuitive point of view: longer microcracks in SWCNT networks hinders the electron pathway and thus increases resistance under stretching (Figure S13, Supporting Information). In addition, we employed the voltage drop simulation on SEM images of auxetic strain sensors under 30% nominal strain, presenting voltage drop faster than 15% strain, since a larger strain results in larger

10

resistance (Figure S14, Supporting Information). It can be concluded from this model that larger microcrack length in auxetic metamaterial sensors leads to sensitivity enhancement, which is in good agreement with experimental results.

In the second simulation, FEA was employed to explain the microcrack elongation resulted from auxetic metamaterials, through stress and strain filed effect. Based on fracture mechanics, the stress concentration would occur at crack tips when service loading increased generally (Figure S15, Supporting Information). Cracks would propagate when the driving force on structures exceeds fracture threshold. Here FEA simulation results showed propagation of a representative microcrack, under stretching loading on auxetic and conventional flat structures respectively (Figure 3g, h). Upon 14.1% normal tensile strain, microcrack within auxetic structure cuts through the width of simulation area completely. In comparison, microcrack with conventional flat structure is obviously shorter under same stretching loading (Figure S16, 17, Supporting Information). The simulation results manifest good consistency with experimental SEM observation. It provides a simple explanation that auxetic metamaterials regulate the propagation of microcracks within SWCNT network.

Combining the aforementioned experimental and simulation results together, the sensitivity improvement of auxetic metamaterial sensors is explained by model of elongated microcracks (Figure 3j). The active material, conductive SWCNT network, can be regarded as SWCNT islands due to the microcracks within it.[22,27,60] In relaxed state, these SWCNT islands contact with each other, thus provides an

11

unblocked electron pathway, corresponding to initial resistance R_0. Under longitudinal tensile strain ε, transverse Poisson compression on SWCNT islands squeezes them together, and thus makes short microcracks (Figure 3i). Alternatively, reduced structural Poisson's ratio of auxetic metamaterial structure decreases transverse Poisson compression, which promotes the separation of SWCNT islands and thus resulting in longer microcracks. As proven in voltage drop simulation, the electron pathway depends on the length of microcracks. Therefore, auxetic strain sensors would provide smaller current than conventional flat ones (blue and orange arrows in Figure 3i, j), indicating large relative resistance change and sensitivity.

To demonstrate the practical application of our highly sensitive stretchable strain sensors based on auxetic metamaterial, human radial artery pulse was detected from a healthy female volunteer. A strain sensor of 5-unit auxetic metamaterial array was attached to human wrist (**Figure 4**a). Due to the high sensitivity, auxetic metamaterial sensor exhibits high signal-to-noise ratio (SNR) of 104.8 dB, while SNR of conventional flat sensors was only 39.4 dB (Figure 4b). Pulse peak can be distinguished from signals of both auxetic and conventional flat sensors (Figure 4c, d). However, only signals from auxetic sensors exhibit discernible medical details within one pulse, providing information of forward wave, peak systolic pressure, discrotic notch and tricuspid valve opening. In comparison, due to low sensitivity, conventional flat sensor only obtains one single beat in pulse profile, losing detailed medical information. These data suggest that our auxetic metamaterial sensors demonstrate great potentials to continuously monitor daily health with high precision

12

and abundant medical details.

In conclusion, we employed auxetic metamaterials to significantly enhance sensitivity of stretchable strain sensors. Instead of the transverse Poisson compression in conventional thin film, auxetic metamaterial frame exhibits bi-directional expansion due to the reduced Poisson's ratio. Compared to conventional sensors, sensitivity is greatly elevated with a 24-fold improvement. This sensitivity enhancement is due to the synergistic effect of reduced structural Poisson's ratio and strain concentration. The underlying mechanism, elongated microcracks, was proven by both experimental results and numerical simulations. Importantly, this study demonstrates a radically new strategy to enhance sensitivity of stretchable strain sensors, which further enables their practical applications. Moreover, our strategy is independent with active materials employed, thus can be utilized to other stretchable strain sensors. Ultimately, this pioneering work brings the whole mechanical metamaterial field into the view of stretchable electronics. The functionalities of stretchable electronics are heavily dependent on mechanical properties under deformation, thus metamaterials with superior mechanical behaviors could inject vitality and build momentum to this field.

Reference

[1]   Z. Bao, X. Chen, *Adv. Mater.* **2016**, *28*, 4177.

[2]   S. Choi, H. Lee, R. Ghaffari, T. Hyeon, D. H. Kim, *Adv. Mater.* **2016**, *28*, 4203.

[3]   C. B. Cooper, K. Arutselvan, Y. Liu, D. Armstrong, Y. Lin, M. R. Khan, J. Genzer, M. D. Dickey, *Adv. Funct. Mater.* **2017**, *27*, 1605630.

[4]   Q. Liao, M. Mohr, X. Zhang, Z. Zhang, Y. Zhang, H.-J. Fecht, *Nanoscale* **2013**, *5*, 12350.

[5]   J. Guo, X. Liu, N. Jiang, A. K. Yetisen, H. Yuk, C. Yang, A. Khademhosseini, X. Zhao, S. H. Yun, *Adv. Mater.* **2016**, *28*, 10244.

[6]   D. Y. Park, D. J. Joe, D. H. Kim, H. Park, J. H. Han, C. K. Jeong, H. Park, J. G. Park, B. Joung, K. J. Lee, *Adv. Mater.* **2017**, *29*, 1702308.

[7]   X. Huang, Y. Liu, H. Cheng, W.-J. Shin, J. A. Fan, Z. Liu, C.-J. Lu, G.-W. Kong, K. Chen, D. Patnaik, S.-H. Lee, S. Hage-Ali, Y. Huang, J. A. Rogers, *Adv. Funct. Mater.* **2014**, *24*, 3846.

[8]   O. Atalay, A. Atalay, J. Gafford, H. Wang, R. Wood, C. Walsh, *Adv. Mater. Technol.* **2017**, *2*, 1700081.

[9]   J. M. Wu, C.-Y. Chen, Y. Zhang, K.-H. Chen, Y. Yang, Y. Hu, J.-H. He, Z. L. Wang, *ACS Nano* **2012**, *6*, 4369.

[10] D. H. Kim, H. J. Shin, H. Lee, C. K. Jeong, H. Park, G.-T. Hwang, H.-Y. Lee, D. J. Joe, J. H. Han, S. H. Lee, J. Kim, B. Joung, K. J. Lee, *Adv. Funct. Mater.* **2017**, *27*, 1700341.

[11] D. Rus, M. T. Tolley, *Nature* **2015**, *521*, 467.

[12] L. Cai, L. Song, P. Luan, Q. Zhang, N. Zhang, Q. Gao, D. Zhao, X. Zhang, M. Tu, F. Yang, W. Zhou, Q. Fan, J. Luo, W. Zhou, P. M. Ajayan, S. Xie, *Sci. Rep.* **2013**, *3*, 3048.

[13] D. J. Cohen, D. Mitra, K. Peterson, M. M. Maharbiz, *Nano Lett.* **2012**, *12*, 1821.

[14] S. Yao, Y. Zhu, *Nanoscale* **2014**, *6*, 2345.

[15] H. Ota, K. Chen, Y. Lin, D. Kiriya, H. Shiraki, Z. Yu, T.-J. Ha, A. Javey, *Nat. Commun.* **2014**, *5*, 5032.

[16] G. Cai, J. Wang, K. Qian, J. Chen, S. Li, P. S. Lee, *Adv. Sci.* **2017**, *4*, 1600190.

[17] H.-l. Yan, Y.-q. Chen, Y.-q. Deng, L.-l. Zhang, X. Hong, W.-m. Lau, J. Mei, D. Hui, H. Yan, Y. Liu, *Appl. Phys. Lett.* **2016**, *109*, 083502.

[18] T. Q. Trung, N. E. Lee, *Adv. Mater.* **2016**, *28*, 4338.

[19] D. Son, J. Lee, S. Qiao, R. Ghaffari, J. Kim, J. E. Lee, C. Song, S. J. Kim, D. J. Lee, S. W. Jun, S. Yang, M. Park, J. Shin, K. Do, M. Lee, K. Kang, C. S. Hwang, N. Lu, T. Hyeon, D. H. Kim, *Nat. Nanotechnol.* **2014**, *9*, 397.

[20] M. Amjadi, K.-U. Kyung, I. Park, M. Sitti, *Adv. Funct. Mater.* **2016**, *26*, 1678.

[21] T. F. O'Connor, M. E. Fach, R. Miller, S. E. Root, P. P. Mercier, D. J. Lipomi, *PLoS One* **2017**, *12*, e0179766.

[22] D. Kang, P. V. Pikhitsa, Y. W. Choi, C. Lee, S. S. Shin, L. Piao, B. Park, K.-Y. Suh, T.-i. Kim, M. Choi, *Nature* **2014**, *516*, 222.

[23] C. Wang, X. Li, E. Gao, M. Jian, K. Xia, Q. Wang, Z. Xu, T. Ren, Y. Zhang, *Adv. Mater.* **2016**, *28*, 6640.

[24] M. Amjadi, A. Pichitpajongkit, S. Lee, S. Ryu, I. Park, *ACS Nano* **2014**, *8*, 5154.

[25] B. Park, J. Kim, D. Kang, C. Jeong, K. S. Kim, J. U. Kim, P. J. Yoo, T.-I. Kim, *Adv. Mater.* **2016**, *28*, 8130.

[26] X. Li, T. Yang, Y. Yang, J. Zhu, L. Li, F. E. Alam, X. Li, K. Wang, H. Cheng, C.-T. Lin, Y. Fang, H. Zhu, *Adv. Funct. Mater.* **2016**, *26*, 1322.

[27] T. Yamada, Y. Hayamizu, Y. Yamamoto, Y. Yomogida, A. Izadi-Najafabadi, D. N. Futaba, K. Hata, *Nat. Nanotechnol.* **2011**, *6*, 296.

[28] Y. Wang, L. Wang, T. Yang, X. Li, X. Zang, M. Zhu, K. Wang, D. Wu, H. Zhu, *Adv. Funct. Mater.* **2014**, *24*, 4666.

[29] E. Roh, B.-U. Hwang, D. Kim, B.-Y. Kim, N.-E. Lee, *ACS Nano* **2015**, *9*, 6252.

[30] I. You, B. Kim, J. Park, K. Koh, S. Shin, S. Jung, U. Jeong, *Adv. Mater.* **2016**, *28*, 6359.

[31] Y. Q. Li, P. Huang, W. B. Zhu, S. Y. Fu, N. Hu, K. Liao, *Sci. Rep.* **2017**, *7*, 45013.

[32] S. Gong, D. T. H. Lai, Y. Wang, L. W. Yap, K. J. Si, Q. Shi, N. N. Jason, T. Sridhar, H. Uddin, W. Cheng, *ACS Appl. Mater. Interfaces* **2015**, *7*, 19700.

[33] J. Liu, T.-M. Fu, Z. Cheng, G. Hong, T. Zhou, L. Jin, M. Duvvuri, Z. Jiang, P. Kruskal, C. Xie, Z. Suo, Y. Fang, C. M. Lieber, *Nat. Nanotechnol.* **2015**, *10*, 629.

[34] J. Zhao, G. Wang, R. Yang, X. Lu, M. Cheng, C. He, G. Xie, J. Meng, D. Shi, G. Zhang, *ACS Nano* **2015**, *9*, 1622.

[35] Y. Liu, Z. Liu, B. Zhu, J. Yu, K. He, W. R. Leow, M. Wang, B. K. Chandran, D. Qi, H. Wang, G. Chen, C. Xu, X. Chen, *Adv. Mater.* **2017**, *29*, 1701780.

[36] X. Xiao, L. Yuan, J. Zhong, T. Ding, Y. Liu, Z. Cai, Y. Rong, H. Han, J. Zhou, Z.

L. Wang, *Adv. Mater.* **2011**, *23*, 5440.

[37] J. Ge, L. Sun, F. R. Zhang, Y. Zhang, L. A. Shi, H. Y. Zhao, H. W. Zhu, H. L. Jiang, S. H. Yu, *Adv. Mater.* **2016**, *28*, 722.

[38] A. Larmagnac, S. Eggenberger, H. Janossy, J. Vörös, *Sci. Rep.* **2014**, *4*, 7254.

[39] C. J. Lee, K. H. Park, C. J. Han, M. S. Oh, B. You, Y. S. Kim, J. W. Kim, *Sci. Rep.* **2017**, *7*, 7959.

[40] D. Qi, Z. Liu, W. R. Leow, X. Chen, *MRS Bull.* **2017**, *42*, 103.

[41] S. P. Lacour, D. Chan, S. Wagner, T. Li, Z. Suo, *Appl. Phys. Lett.* **2006**, *88*, 204103.

[42] J.-H. Lee, J. P. Singer, E. L. Thomas, *Adv. Mater.* **2012**, *24*, 4782.

[43] K. Bertoldi, V. Vitelli, J. Christensen, M. van Hecke, *Nat. Rev. Mater.* **2017**, *2*, 17066.

[44] Y. Gao, W. Yang, B. Xu, *Adv. Mater. Interfaces* **2017**, *4*, 1700278.

[45] Y. Liu, K. He, G. Chen, W. R. Leow, X. Chen, *Chem. Rev.* **2017**, *117*, 12893.

[46] Z. G. Nicolaou, A. E. Motter, *Nat. Mater.* **2012**, *11*, 608.

[47] J. L. Silverberg, A. A. Evans, L. McLeod, R. C. Hayward, T. Hull, C. D. Santangelo, I. Cohen, *Science* **2014**, *345*, 647.

[48] A. Rafsanjani, A. Akbarzadeh, D. Pasini, *Adv. Mater.* **2015**, *27*, 5931.

[49] L. R. Meza, S. Das, J. R. Greer, *Science* **2014**, *345*, 1322.

[50] X. Zheng, H. Lee, T. H. Weisgraber, M. Shusteff, J. DeOtte, E. B. Duoss, J. D. Kuntz, M. M. Biener, Q. Ge, J. A. Jackson, S. O. Kucheyev, N. X. Fang, C. M. Spadaccini, *Science* **2014**, *344*, 1373.

[51] H. M. A. Kolken, A. A. Zadpoor, *RSC Adv.* **2017**, *7*, 5111.

[52] T. Li, Z. Huang, Z. Suo, S. P. Lacour, S. Wagner, *Appl. Phys. Lett.* **2004**, *85*, 3435.

[53] Y.-Y. Lee, J.-H. Lee, J.-Y. Cho, N.-R. Kim, D.-H. Nam, I.-S. Choi, K. T. Nam, Y.-C. Joo, *Adv. Funct. Mater.* **2013**, *23*, 4020.

[54] J. A. Rogers, T. Someya, Y. Huang, *Science* **2010**, *327*, 1603.

[55] M. Kaltenbrunner, M. S. White, E. D. Głowacki, T. Sekitani, T. Someya, N. S. Sariciftci, S. Bauer, *Nat. Commun.* **2012**, *3*, 770.

[56] T. Sekitani, H. Nakajima, H. Maeda, T. Fukushima, T. Aida, K. Hata, T. Someya, *Nat. Mater.* **2009**, *8*, 494.

[57] Z. Liu, D. Qi, P. Guo, Y. Liu, B. Zhu, H. Yang, Y. Liu, B. Li, C. Zhang, J. Yu, B. Liedberg, X. Chen, *Adv. Mater.* **2015**, *27*, 6230.

[58] A. Chortos, Z. Bao, *Mater. Today* **2014**, *17*, 321.

[59] W. Cao, P. Görrn, S. Wagner, *Appl. Phys. Lett.* **2011**, *98*, 212112.

[60] I. M. Graz, D. P. J. Cotton, S. P. Lacour, *Appl. Phys. Lett.* **2009**, *94*, 071902.
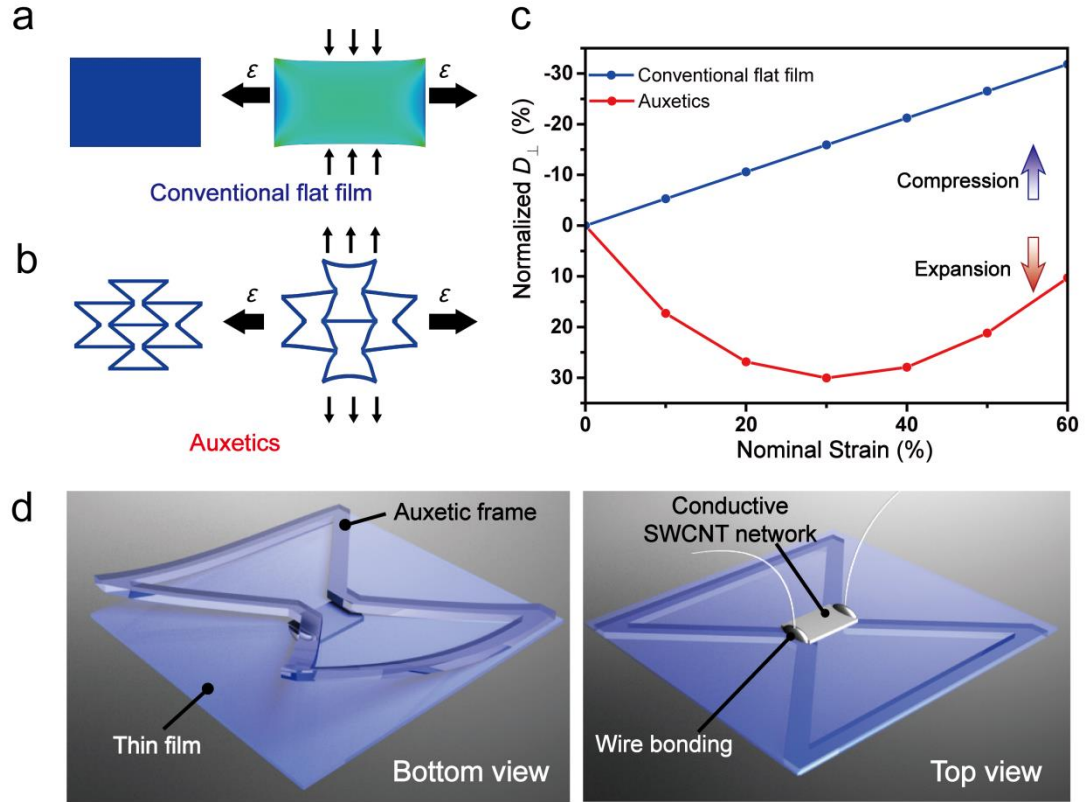
Scheme 1. Stretchable strain sensors based on auxetic mechanical metamaterials. a) Conventional flat film structure and b) auxetic metamaterial structure with 4-unit array, with corresponding deformation under 15% tensile strain from FEA simulation. c) Normalized displacement in transverse direction ($D_\perp$) under longitudinal tensile strain. Negative and positive $D_\perp$ represents transverse Poisson compression and transverse auxetic expansion respectively. d) Illustration diagram of stretchable strain sensors based on auxetic metamaterials, which is composed of: auxetic frame, thin film and conductive SWCNT network.
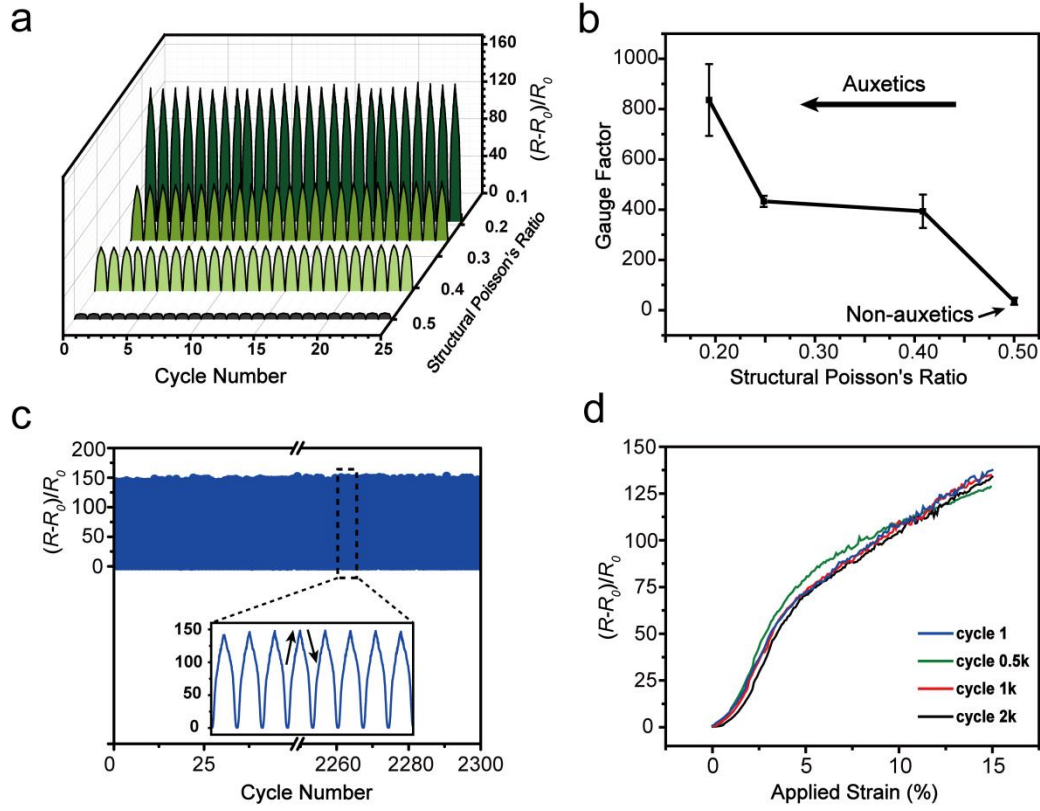
Figure 1. Performance of stretchable strain sensors based on auxetic metamaterials, and regulatory role of structural Poisson's ratio. a) Relative resistance change and b) average gauge factor under 25 tensile cycles, demonstrating sensitivity enhancement by auxetic structures. c) Cyclic durability test of 2,300 cycles under 15% tensile strain (structural Poisson's ratio of 0.19). Inset demonstrates enlarged vision, with the "up" and "down" arrows showing loading and unloading process respectively. d) Relative resistance change of different cycles, with high similarity.
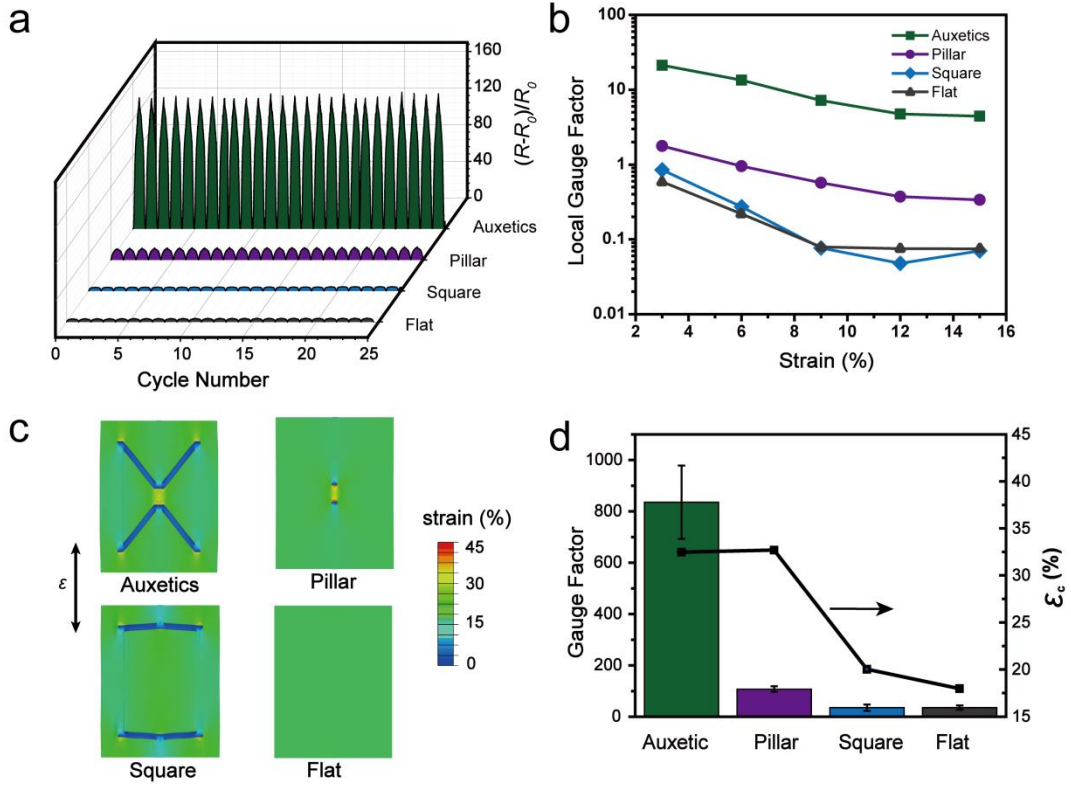
Figure 2. Sensitivity within various strain range, and regulatory role of strain re-distribution and concentration. a) Relative resistance change curves of auxetic and three non-auxetic strain sensors (pillar, square and flat). b) Local gauge factor as the slope of relative resistance change curves, showing sensitivity advantages of auxetic strain sensors in various strain range. c) Strain distribution from FEA simulation, under 15% nominal strain. d) Average gauge factor and strain concentration ε_c in conductive SWCNT area (resistance testing area).
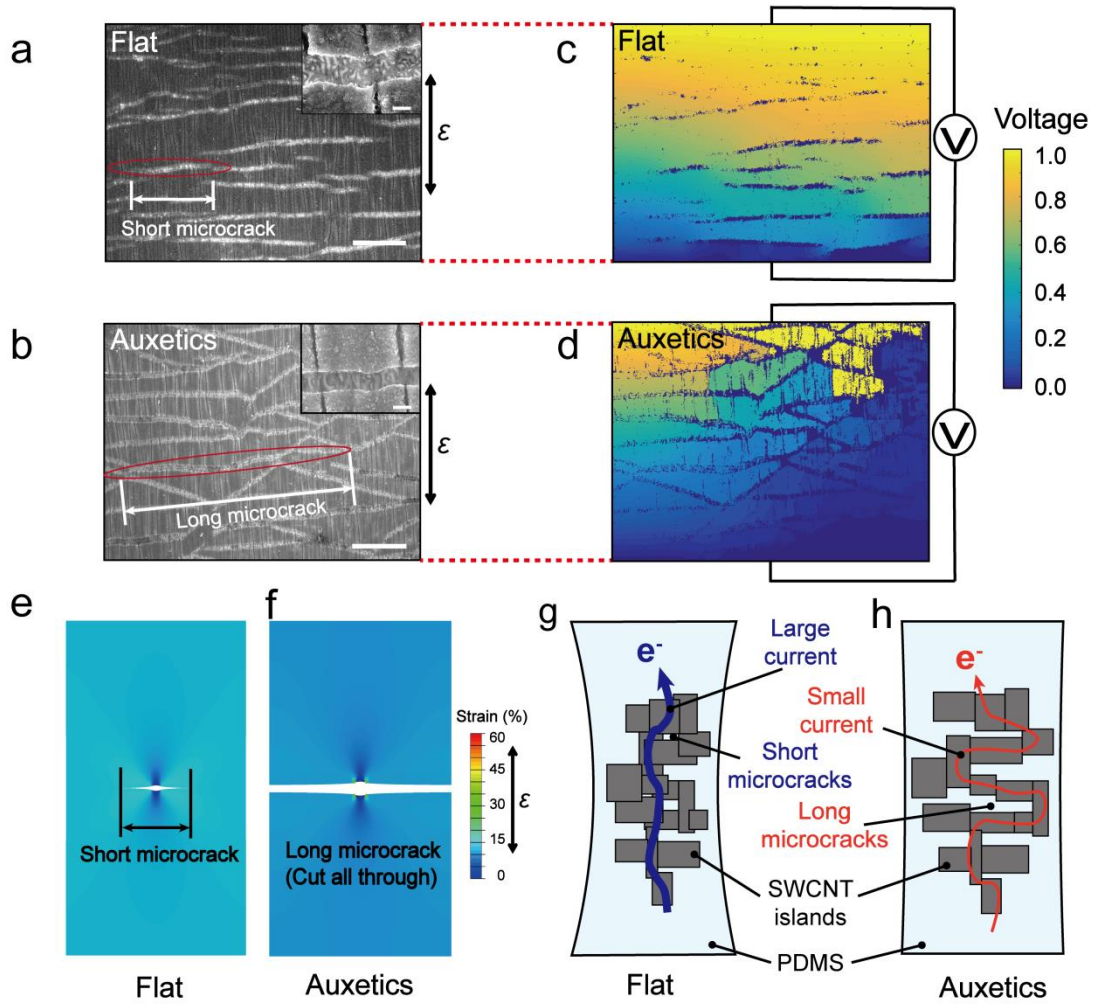
Figure 3. Microcracks within stretchable strain sensors based on auxetic and conventional flat structures. a, b) SEM images of microcracks within SWCNT layer, under 15% nominal strain. Scale bar: (a, b) 10 μm, Insets 500 nm. c, d) Voltage distribution simulation, based on experimental SEM images. Auxetic strain sensors exhibit fast voltage drop and thus large resistance, consistent with their high sensitivity. e, f) Propagation of single microcrack under 14.1% tensile strain from FEA simulation. Longer microcrack occurs in stretchable strain sensors based on auxetic metamaterials, consistent with experimental SEM images. g, h) Microcrack

model of stretchable strain sensors, explaining gauge factor enhancement induced by auxetic metamaterial structure.
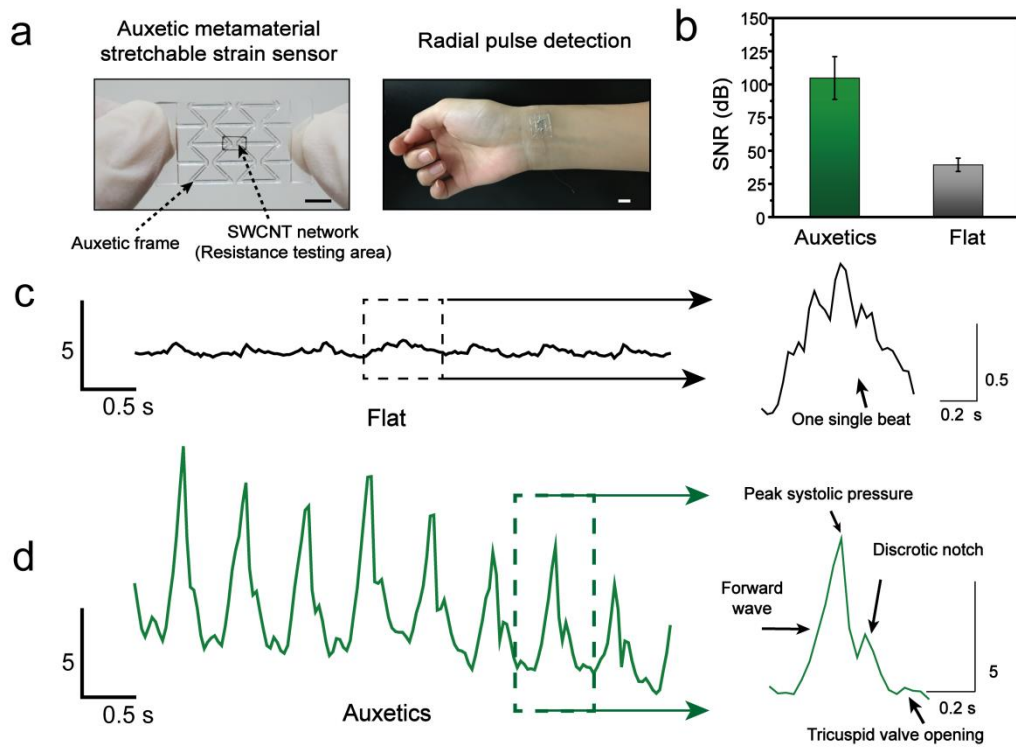
Figure 4. Detection of human radial pulse wave, using stretchable strain sensors based on auxetic and conventional flat structures. a) Photograph of stretchable strain sensor with 5-unit auxetic array (Scale bar: 5 mm), and sensor attaching to human wrist for radial pulse detection (Scale bar: 1 cm). The SWCNT network inside the ring is thin enough to be transparent. b) Signal-to-noise ratio (SNR) comparison of auxetic and conventional flat sensors. c, d) Human radial pulse profiles, in which enlarged signal from auxetic strain sensor shows discernible stages and abundant medical details, due to its high sensitivity.

The table of contents entry

Auxetic mechanical metamaterials have been employed to significantly enhance sensitivity of stretchable strain sensors, by regulating transverse Poisson effect due to auxetic expansion. High sensitivity with almost 24-fold improvement is achieved, together with high maximum stretchability and cyclic durability. Additionally, the underlying mechanism, elongated microcracks, is proven by both experiments and numerical simulations.

Auxetic Mechanical Metamaterials to Enhance Sensitivity of Stretchable Strain Sensors

Ying Jiang, Zhiyuan Liu, Naoji Matsuhisa, Dianpeng Qi, Wan Ru Leow, Hui Yang, Jiancan Yu, Geng Chen, Yaqing Liu, Changjin Wan, Zhuangjian Liu,* Xiaodong Chen*

ToC figure
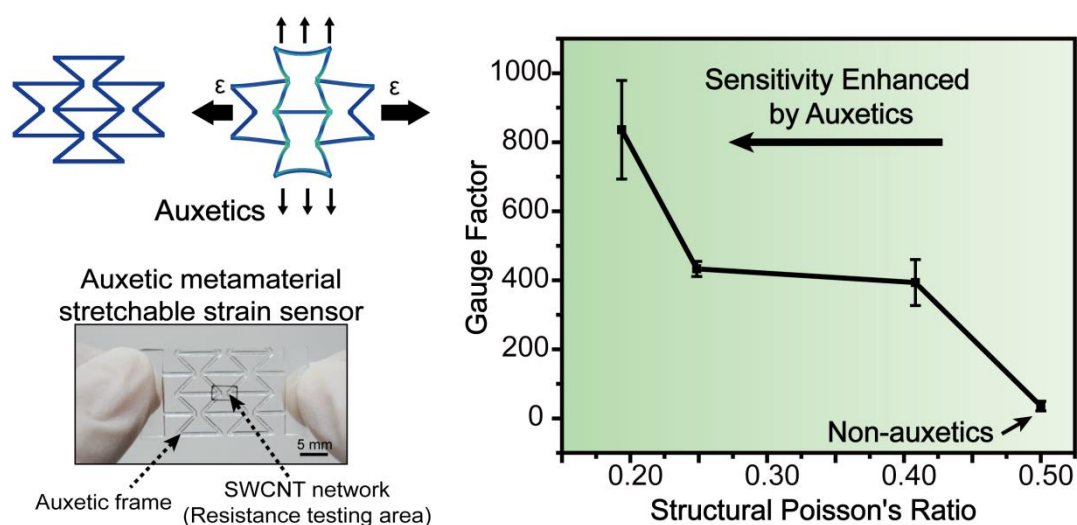
Auxetic Mechanical Metamaterials to Enhance Sensitivity of Stretchable Strain Sensors

Ying Jiang, Zhiyuan Liu, Naoji Matsuhisa, Dianpeng Qi, Wanru Leow, Hui Yang, Jiancan Yu, Geng Chen, Yaqing Liu, Changjin Wan, Zhuangjian Liu,* Xiaodong Chen*
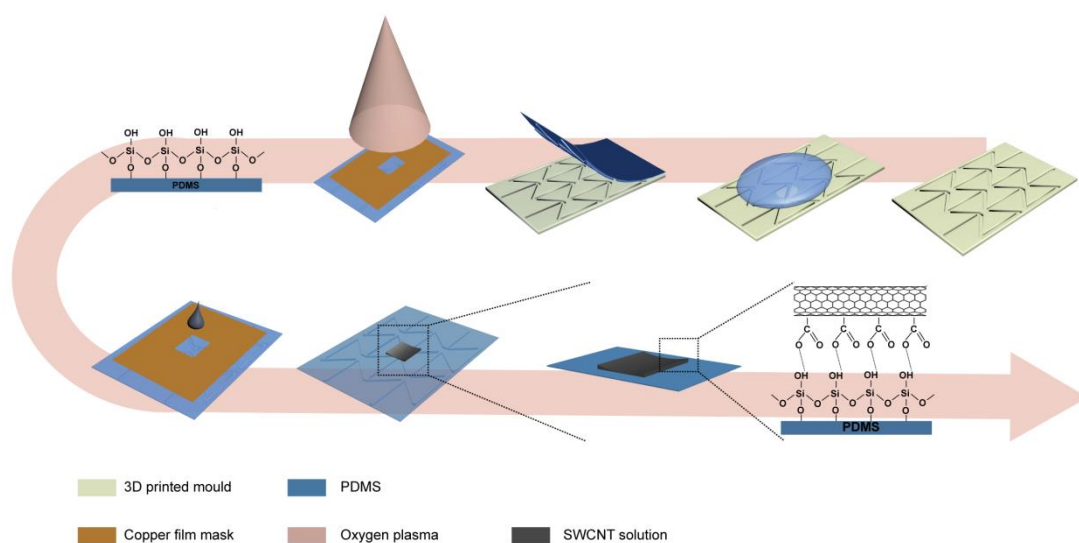

Figure S1. Illustration of the fabrication method for stretchable strain sensors based on auxetic metamaterials.
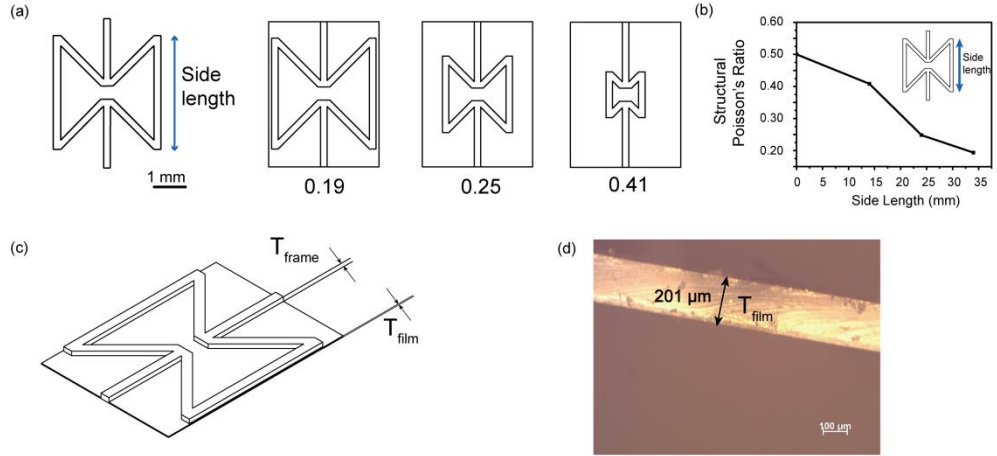
Figure S2. a) Illustration of the basic unit (bow-tie shape) in auxetic metamaterial structure. Auxetic structures with different side length represent different structural Poisson's ratio, of 0.19, 0.25 and 0.41 respectively. b) Tuning structural Poisson's ratio by changing side length. c) The total thickness of device T_{device} is the sum of auxetic frame thickness T_{frame} and thin film thickness T_{film}. Here T_{frame} is set to be 1 mm, which can be precisely controlled by 3D printing model. d) Optical microscope of cross section of auxetic strain sensor, showing thin film thickness T_{film} of 201 µm.
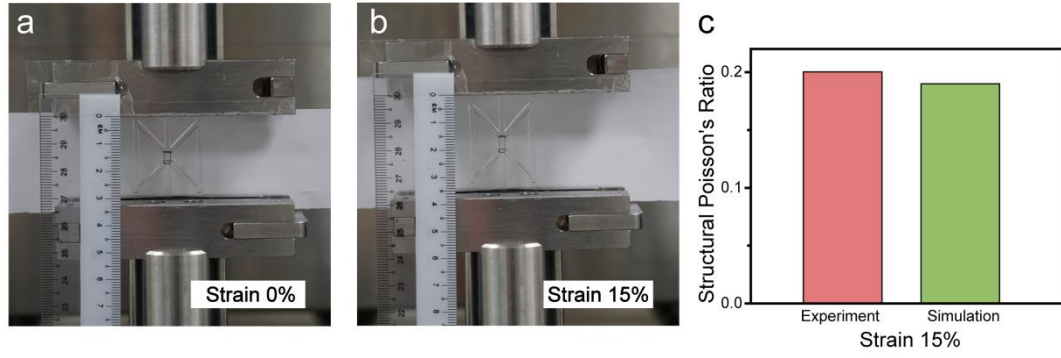
Figure S3. a, b) Actual photo images for auxetic metamaterial-based stretchable strain sensors with structural Poisson's ratio of 0.19, before and after 15% nominal strain. c) By using open-code image analyzing software ImageJ, the structural Poisson's ratio in SWCNT area of auxetic strain sensor was calculated to be 0.200 at 15% strain, which is consistent with the FEA calculation.
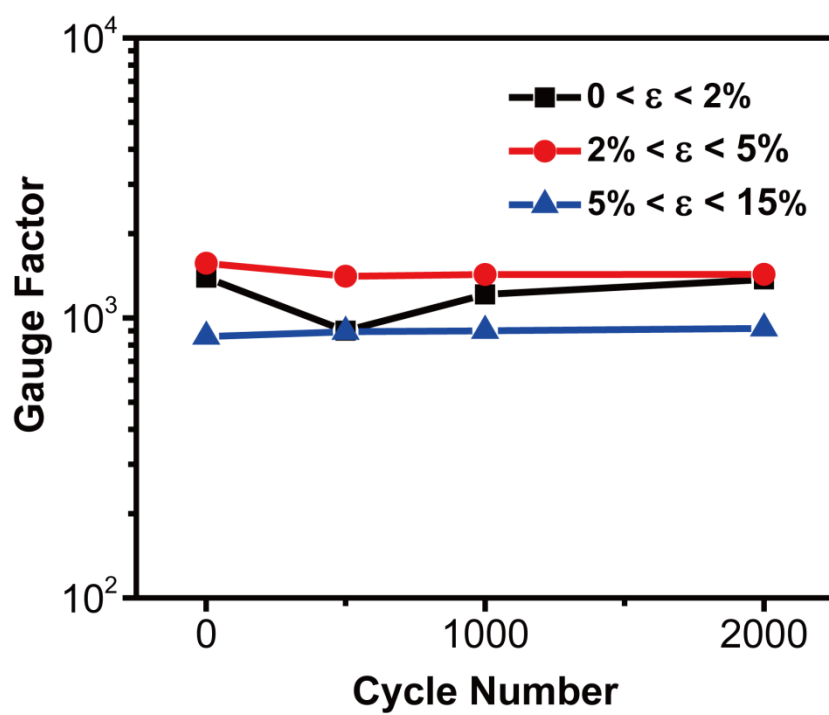
Figure S4. Gauge factor in different cycles and strain ranges, showing high sensitivity even under large strain.
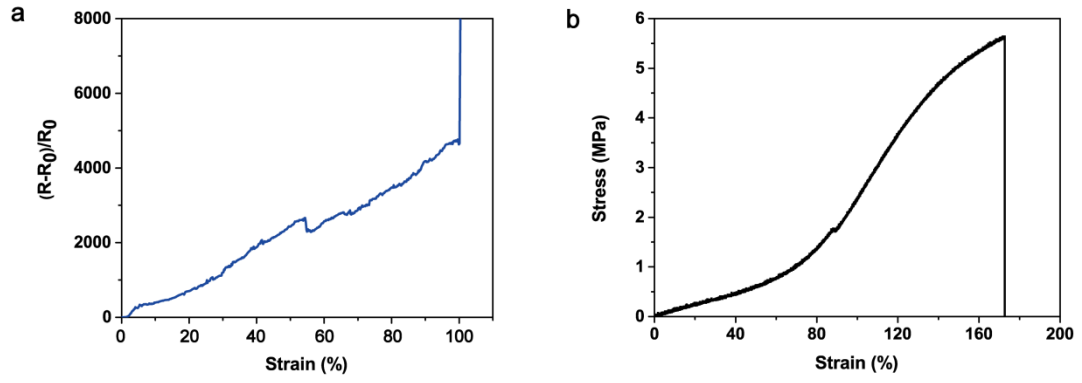
Figure S5. a) Stretchability of stretchable strain sensors based on auxetic metamaterials, with maximum strain of 98%. Noise in large strain range comes from wire bonding and sample clamping. b) Stress-strain curve of flat PDMS film, with stretchability of >160%.
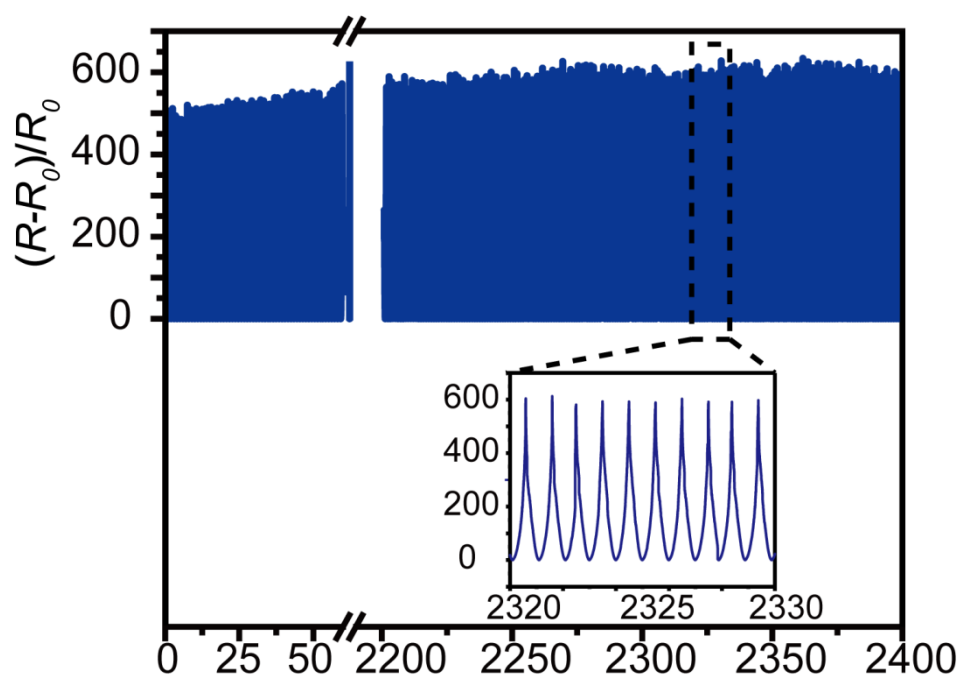
Figure S6. Cyclic durability test of 2,400 cycles under 30% tensile strain (structural Poisson's ratio of 0.19). The maximum relative resistance change increased a little during first 50 cycles, since the microcrack pattern in SWCNT layer has not been completely finalized. The relative resistance change curve kept stable even after 2,200 cycles, while maximum relative resistance change reached ~580, showing good cyclic durability under 30% tensile strain.
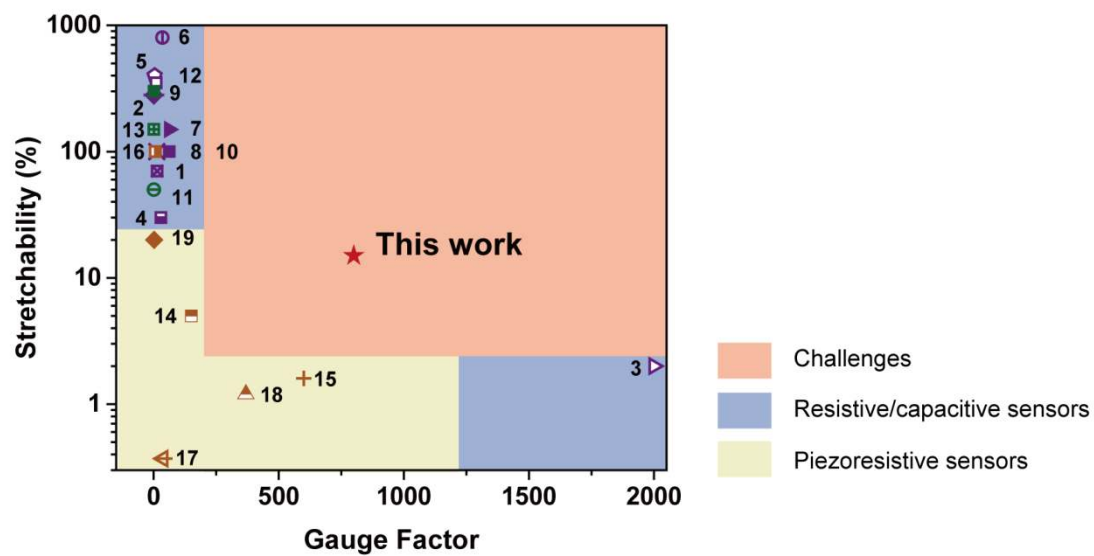
Figure S7. Performance comparison with other stretchable strain sensors reported in the literature.[1-19]
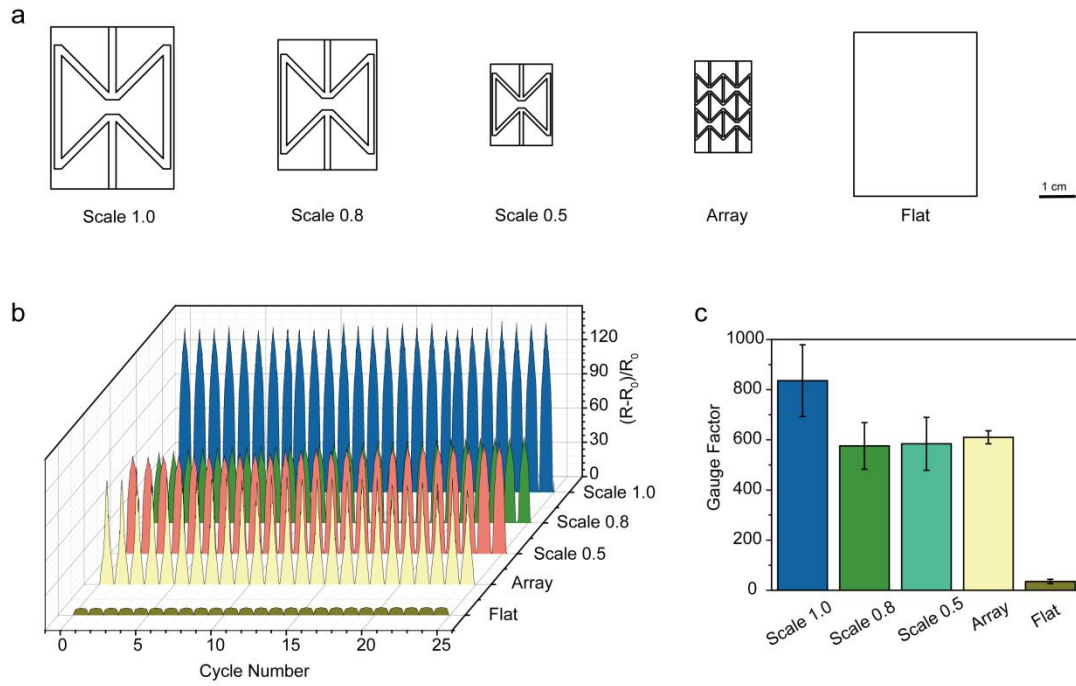
Figure S8. a) Illustration diagrams, b) relative resistance change within 25 tensile cycles, and c) average gauge factor of different stretchable strain sensors. Scaling 1.0, 0.8, 0.5 represent sensors with dimensions scaled down to corresponding values. In this case, the final volume were scaled down to 1, 0.512 and 0.125 of original volume, with thickness of auxetic frame T_{frame} of 1000 μm, 800 μm and 500 μm respectively. Array sensor represents 5-unit auxetic array, where in each unit dimension in x, y axis was 0.25 of original value, and thickness of auxetic frame is 0.5 of original value. In this case, final volume of each unit in array sensor was reduced to 0.03125 of original volume, with T_{frame} of 500 μm.
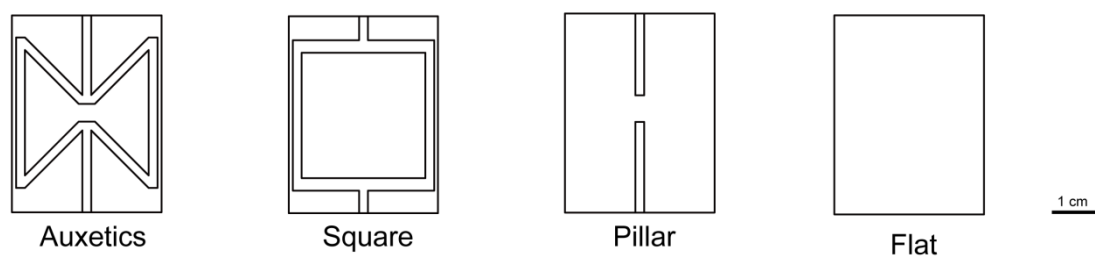
Figure S9. Illustration diagrams of auxetic metamaterial structure, and non-auxetic control with square, pillar and flat structures.
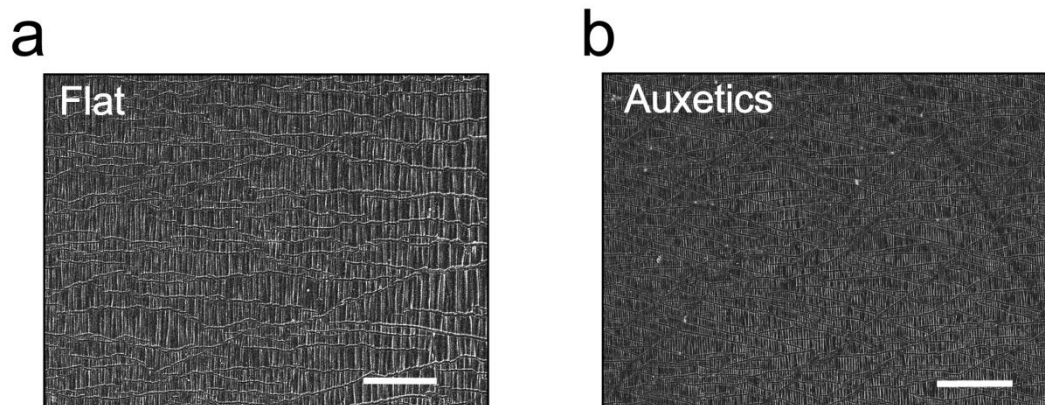
Figure S10. SEM images of stretchable strain sensors based on auxetic metamaterials and flat structures, under 30% nominal tensile strain.   Scale bar: 40 μm.
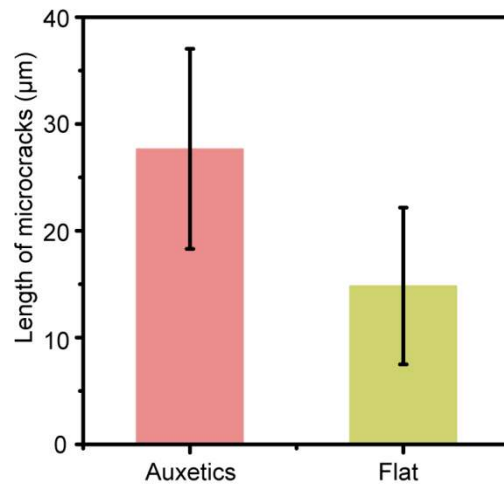
Figure S11. Average microcrack length in auxetic and conventional flat strain sensors under 15% tensile strain, calculated from SEM images.
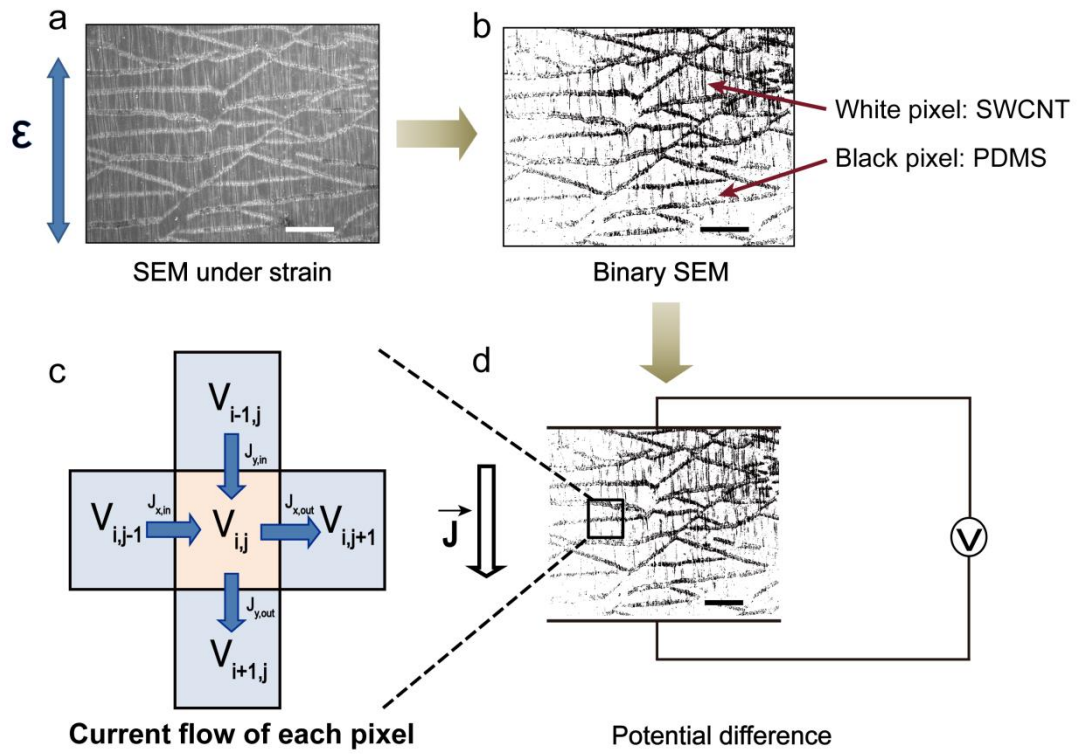
Figure S12. Flow chart of voltage drop simulation based on experimental SEM images. a) SEM image of microcracks in strain sensors based on auxetic metamaterials, under 15% tensile strain. b) Converted binary SEM, with white and black pixels representing conductive SWCNT and insulating cracks, respectively. c) Current flow of pixel $V_{i,j}$ with the neighboring pixels. d) Applied potential difference (1 V) on both top and down sides, as the matrix boundary condition (Scale bar: 10 μm).
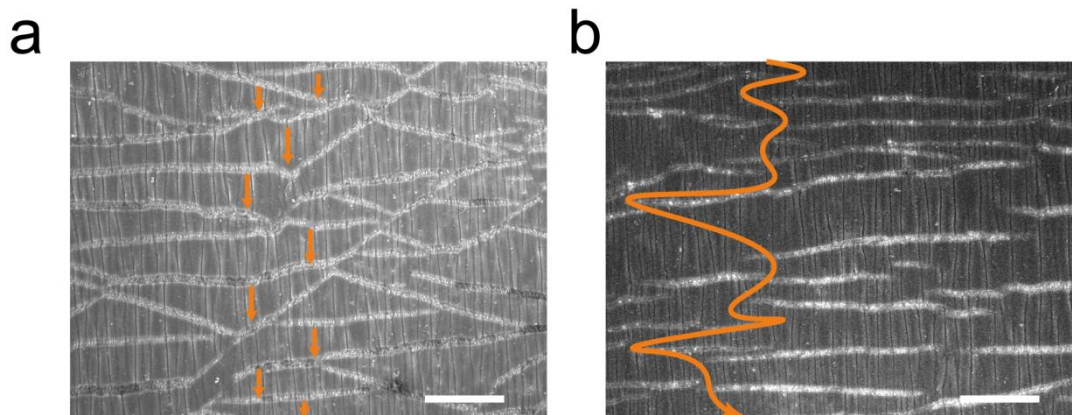
Figure S13. Intuitive electron pathway (shown in orange arrows) in SEM images of auxetic and conventional flat sensors respectively (Scale bar: 10 μm).
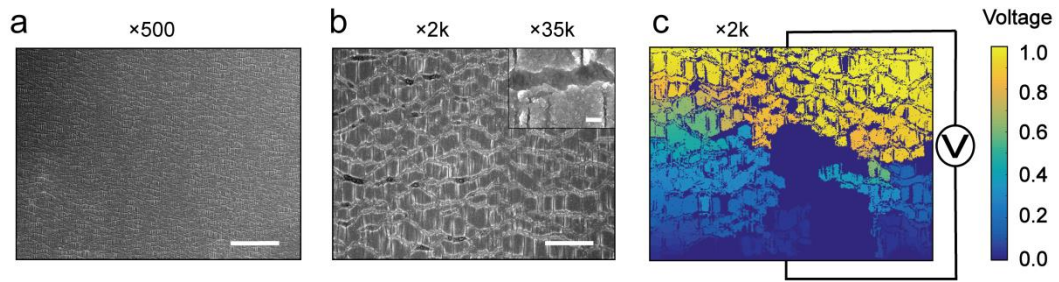
Figure S14. Microcracks in auxetic strain sensors under 30% nominal strain.   a, b) SEM images with different magnification.   Scale bar: a) 40 μm, b) 10 μm, Inset: 500 nm.   c) Voltage distribution simulation based on experimental SEM images of ×2k magnification, presenting fast voltage drop.
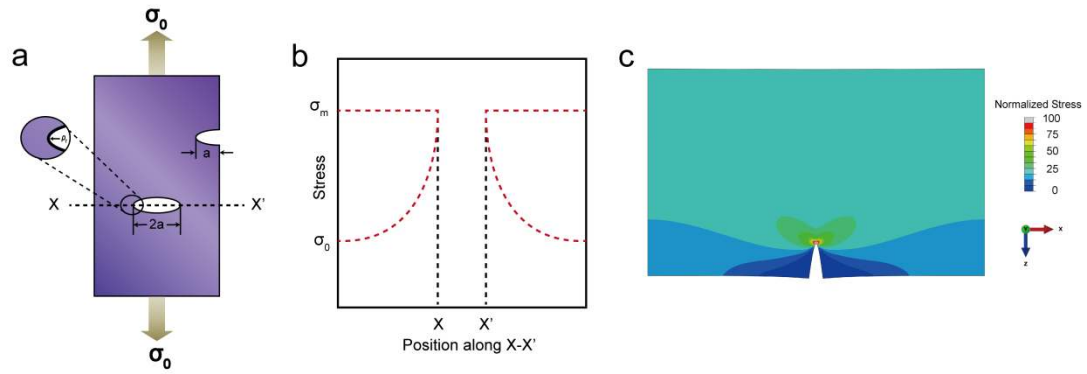
Figure S15. a, b) Illustration of stress concentration along a specimen with a crack. σ_m, σ_0, α and ρ_t represent the maximum stress at crack tip area, nominal applied tensile stress, half length of crack, and radius of curvature at crack tip, respectively. c) Stress concentration at crack tip area, from FEA simulation.
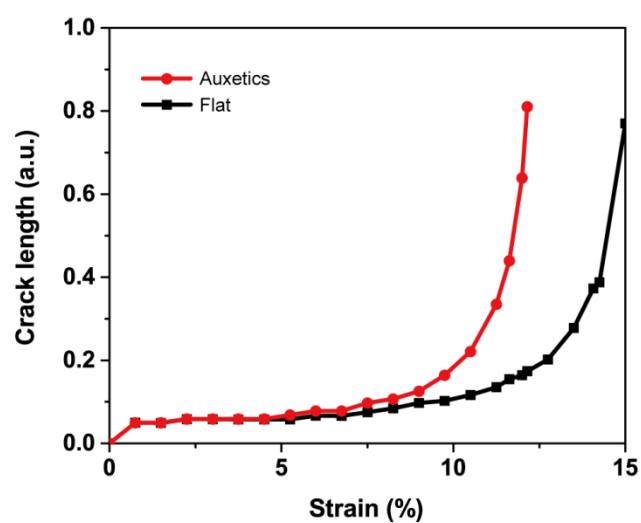
Figure S16. Crack length (a.u.) within auxetic and conventional flat sensors under different tensile strain, from FEA simulation. A small initial crack was employed in both FEA models to enable crack propagation, resulting in similar crack length in small strain range (<5%).
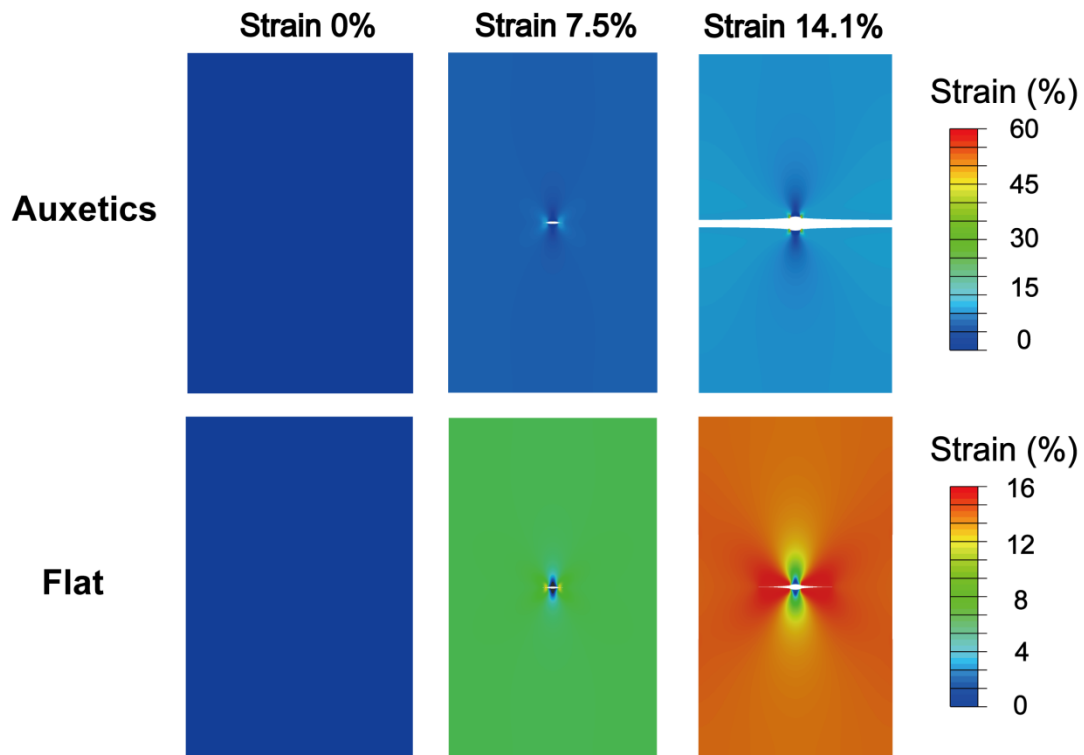
Figure S17. Illustration of microcrack length and strain distribution in auxetic and conventional flat stretchable strain sensors, under 0%, 7.5% and 14.1% tensile strain, from FEA simulation.

Experimental Section

Fabrication of 3D printed auxetic mold: Inverse patterns of auxetic metamaterials or non-auxetic structures are printed out by 3D printer (Eden260VS, Stratasys Co.) via digital UV light curing. Veroclear (RGD810, Stratasys Co.) was used as mold material, and SUP705 (Stratasys Co.) as soluble supporting material, which was washed away immediately after 3D printing process.

Fabrication of stretchable strain sensor based on auxetic metamaterials: Monomer and cross linker of poly(dimethyl siloxane) (PDMS, Sylgard 184) were mixed together at ratio of 10:1, stirred by stick and defoamed by centrifuge. Then PDMS precursor was poured into 3D printed mold, and cured in 40 $^{\circ}$C oven for 1 day. After peeling off, the PDMS auxetic frame and thin film were successfully fabricated together. To cast a conductive thin layer on the PDMS thin film, single wall carbon nanotube solution (P3-SWCNT, Carbon Solutions Inc.) was prepared by dispersing SWCNT in de-ionized water with 0.5 mg/ml. The solution was ultrasonicated (Fisher Scientific FB15051) for 2 days, and placed for around two hours for stabilization, and only the supernatant solution was used.

Hollow masks with certain patterns to define hydrophilic area on PDMS thin film were fabricated by lithography method. A PET lithography shadow mask was printed by a normal inject printer (HP LaserJet M4345 mfp PCL6). Four sheets of PET with the same patterns were stacked together to prevent UV light permeation. Then photoresist (AZ1518) was spin coated upon Cu foil on glass substrate, at 3000

rpm for 60 seconds.   Then standard photoetching procedure was executed.   After development, the Cu foil was etched by 1 mol/L FeCl$_3$ solution, making a hollow Cu mask with designed pattern.   The hollow Cu masks were put on top of PDMS thin film, and oxygen plasma was applied with pressure of 5 mbar, 50% of power, and 0.5 minutes.   10 µL of SWCNT solution were dropped on hydrophilic area, and dried in room temperature.

Synchronous electro-mechanical characterization: Wire bonding from the stretchable strain sensors was achieved by using liquid metal (Gallium-indium eutectic, Aldrich) on both sides of the conductive SWCNT network, with initial resistance of ~1.0 kΩ. Common copper wires were used to connect liquid metal to Keithley 4200-SCS for resistance measurement.   Tensile machine (Instron 5848) with a customized oven was employed to apply tensile tests, at speed of 0.1 mm/s.   Microcrack pattern in SWCNT layer is not finalized during first few cycles, which will lead to unstable electrical performance.   Therefore, all the electro-mechanical testing was conducted after warm-up cycles (usually 50-200 cycles), to achieve stable performance.

Scanning electron microscopy: Stretchable strain sensors were stretched to 15% nominal strain and glued to a glass slide by AB glue.   The scanning electron microscope was conducted by Field Emission Scanning Electron Microscopy (FESEM, JEOL JSM-7600F), without additional conductive coating.

Strain distribution from FEA simulation: Finite element analysis (FEA) is employed to analyze the strain distribution of stretchable strain sensors based on auxetic metamaterials under stretching. Four different designs of stretchable strain sensor were simulated: auxetics, pillar, square and flat.

Due to the structural symmetry of the stretchable strain sensors, a 1/4 representative part was simulated, and full contour results for whole device were conducted in post-process. The PDMS structures were modeled with the same size as experimental specimen. SWCNT conductive network was modeled as a thin sheet contacted on the middle of PDMS thin film, also with the same size as in experiments ($4*6$ mm^2).

In this FEA simulation, the large strain nonlinear behavior of PDMS was modeled as hyperelastic material by two term Mooney-Rivlin Model, with C_{10}=0.3378, C_{01}=0.0834, D_1=0.0096. The value of constants C_{10}, C_{01} and D_1 were determined by curve-fitting of stress-strain curves from experiment (Figure S5b, Supporting Information). The density of PDMS was set as $9.7*10^{-10}$ tonne/mm^3. SWCNT was modeled as isotropic elastic material, with Young's modulus of 300 MPa. The boundary conditions are set as free in X and Z directions and nominal strain was applied in Y direction. From the FEA simulation result, the strain distribution in auxetic sample shows an obvious strain concentration in the conductivee SWCNT region, with >30% peak strain (maximum principle strain).

Resistance model simulation: This phenomenological model was based on a previous

work of Wagner's group.[20]   It qualitatively explains why longer microcracks lead to higher resistance, which results in high sensitivity of stretchable strain sensors.

Firstly, experimental SEM images of auxetic and conventional flat sensors are binarized from gray scale to black-and-white color (Figure S12a, b, Supporting Information).   Black and white pixels represent exposed PDMS in microcracks (non-conductive area) and SWCNT network (conductive area), respectively.   The criterion of binarization is:

$$\sigma_{i,j} = f(x) = \begin{cases} 1, & x < threshold \\ 0, & x \geq threshold \end{cases}$$

where x means the gray scale of original SEM image pixel, (i,j) means the serial number of pixel, and $\sigma_{i,j}$ means the converted binary value.   Threshold value was chosen on criterion that the converted binary SEM has the same microcrack pattern as original SEM.   Thirdly, we apply an electrical potential difference on two sides of the binary SEM images, which can be regarded as a Dirichlet-type boundary (Figure S12d, Supporting Information).   In this case, current flow of each pixel obeys the continuity condition:

$$J_{x,in} + J_{x,out} + J_{y,in} + J_{y,out} = 0$$

where J is the surface current density.   Discretized Ohm's law was also employed to solve electrical current of each pixel.   Finally, potential of each pixel can be solved from this matrix formula:

$$Ax=b$$

where A contains conductive information $\sigma_{i,j}$ of each pixel, x contains the potential distribution information, and b contains boundary condition information (applied

potential drop). By solving matrix problem by Matlab software, potential distribution x of SEM images can be obtained.   In our case, potential drop are faster in auxetic strain sensors than conventional flat ones, which phenomenologically verified the improved sensitivity enhancement by auxetic metamaterials.

Crack length from FEA simulation: FEA simulation was conducted to qualitatively explain the variations of microcracks in auxetic metamaterial stretchable strain sensors.   A representative area with single microcrack was modeled.   A small initial crack was employed in the center, and the remaining midline was connected by contact interaction property, with damage condition of maximum normal stress (41 MPa), shear stress (41 MPa) and fracture energy (100 mJ).   Material properties were set the same as in previous FEA simulation for strain and stress analysis.   In both models of auxetic metamaterial and conventional flat sensor, the displacement was applied on the ends, which are equivalent to 0%, 7.5%, 15% nominal strain.   The difference between auxetic and flat sensor was shown in boundary conditions: free boundaries represents free Poisson compression, while fixed boundaries represents limited transverse effect by auxetic structure.   The crack of auxetic strain sensors in this FEA cut through the whole simulated area at 14.1% nominal strain.   For fair comparison, final crack length of conventional flat sensor in FEA was also taken at 14.1% nominal strain.

Supporting Reference

[1] M. Amjadi, A. Pichitpajongkit, S. Lee, S. Ryu, I. Park, *ACS Nano* **2014**, *8*, 5154.

[2] T. Yamada, Y. Hayamizu, Y. Yamamoto, Y. Yomogida, A. Izadi-Najafabadi, D. N. Futaba, K. Hata, *Nat. Nanotechnol.* **2011**, *6*, 296.

[3] D. Kang, P. V. Pikhitsa, Y. W. Choi, C. Lee, S. S. Shin, L. Piao, B. Park, K.-Y. Suh, T.-i. Kim, M. Choi, *Nature* **2014**, *516*, 222.

[4] N. Lu, C. Lu, S. Yang, J. Rogers, *Adv. Funct. Mater.* **2012**, *22*, 4044.

[5] J. T. Muth, D. M. Vogt, R. L. Truby, Y. Mengüç, D. B. Kolesky, R. J. Wood, J. A. Lewis, *Adv. Mater.* **2014**, *26*, 6307.

[6] C. S. Boland, U. Khan, C. Backes, A. O'Neill, J. McCauley, S. Duane, R. Shanker, Y. Liu, I. Jurewicz, A. B. Dalton, J. N. Coleman, *ACS Nano* **2014**, *8*, 8819.

[7] S. Gong, D. T. H. Lai, Y. Wang, L. W. Yap, K. J. Si, Q. Shi, N. N. Jason, T. Sridhar, H. Uddin, W. Cheng, *ACS Appl. Mater. Interfaces* **2015**, *7*, 19700.

[8] B.-U. Hwang, J.-H. Lee, T. Q. Trung, E. Roh, D.-I. Kim, S.-W. Kim, N.-E. Lee, *ACS Nano* **2015**, *9*, 8801.

[9] S. Gong, D. T. H. Lai, B. Su, K. J. Si, Z. Ma, L. W. Yap, P. Guo, W. Cheng, *Adv. Electron. Mater.* **2015**, *1*, 1400063.

[10] E. Roh, B.-U. Hwang, D. Kim, B.-Y. Kim, N.-E. Lee, *ACS Nano* **2015**, *9*, 6252.

[11] D. J. Lipomi, M. Vosgueritchian, B. C. K. Tee, S. L. Hellstrom, J. A. Lee, C. H. Fox, Z. Bao, *Nat. Nanotechnol.* **2011**, *6*, 788.

[12] L. Cai, L. Song, P. Luan, Q. Zhang, N. Zhang, Q. Gao, D. Zhao, X. Zhang, M.

Tu, F. Yang, W. Zhou, Q. Fan, J. Luo, W. Zhou, P. M. Ajayan, S. Xie, *Sci. Rep.* **2013**, *3*, 3048.

[13] U.-H. Shin, D.-W. Jeong, S.-M. Park, S.-H. Kim, H. W. Lee, J.-M. Kim, *Carbon* **2014**, *80*, 396.

[14] X.-W. Fu, Z.-M. Liao, J.-X. Zhou, Y.-B. Zhou, H.-C. Wu, R. Zhang, G. Jing, J. Xu, X. Wu, W. Guo, D. Yu, *Appl. Phys. Lett.* **2011**, *99*, 213107.

[15] J. Zhao, G. Wang, R. Yang, X. Lu, M. Cheng, C. He, G. Xie, J. Meng, D. Shi, G. Zhang, *ACS Nano* **2015**, *9*, 1622.

[16] C. Yan, J. Wang, W. Kang, M. Cui, X. Wang, C. Y. Foo, K. J. Chee, P. S. Lee, *Adv. Mater.* **2014**, *26*, 2022.

[17] J. Zhao, C. He, R. Yang, Z. Shi, M. Cheng, W. Yang, G. Xie, D. Wang, D. Shi, G. Zhang, *Appl. Phys. Lett.* **2012**, *101*, 063112.

[18] N. Liu, G. Fang, J. Wan, H. Zhou, H. Long, X. Zhao, *J. Mater. Chem.* **2011**, *21*, 18962.

[19] J. Lee, S. Kim, J. Lee, D. Yang, B. C. Park, S. Ryu, I. Park, *Nanoscale* **2014**, *6*, 11932.

[20] W. Cao, P. Görrn, S. Wagner, *Appl. Phys. Lett.* **2011**, *98*, 212112.